



Article

Amorphous Steel Coatings Deposited by Cold-Gas Spraying

Mario Tului ¹, Cecilia Bartuli ^{2,*}, Alessia Bezzon ¹, Angelo Luigi Marino ¹, Francesco Marra ², Susanna Matera ¹ and Giovanni Pulci ²

¹ Centro Sviluppo Materiali S.p.A. and Lamezia Terme (CZ) Branch Office—Italy, Zona Industriale San Pietro Lametino, 88046 Lamezia Terme (CZ), Italy; mario.tului@rina.org (M.T.); alessia.bezzon@rina.org (A.B.); angelo.marino@rina.org (A.L.M.); susanna.matera@rina.org (S.M.)

² LIMS, INSTM Reference Laboratory for Engineering of Surface Treatments, Department of Chemical Engineering Materials Environment, Sapienza University of Rome, Via Eudossiana 18, 00184 Rome, Italy; francesco.marra@uniroma1.it (F.M.); giovanni.pulci@uniroma1.it (G.P.)

* Correspondence: cecilia.bartuli@uniroma1.it; Tel.: +39-06-44585633

Received: 23 May 2019; Accepted: 7 June 2019; Published: 12 June 2019



Abstract: Cold-gas spray (CGS) deposition of amorphous steel coatings starting from a commercial feedstock powder containing boron, tungsten, and silicon was investigated. Microstructural characterization, carried out by X-ray diffraction (XRD), transmission electron microscopy, and backscattered electron diffraction (EBSD) analysis, confirmed the amorphous nature of deposited coatings. The amorphization phenomenon is related to high-strain/strain-rate deformation with shear instability caused by very high particle kinetic energy, with a mechanism that resembles the severe plastic deformation process. The CGS coatings were heat-treated at temperatures ranging from 650 to 850 °C to induce partial recrystallization. The effect of nanocrystal nucleation and growth on the hardness of the coatings was investigated, and the hardness of heat-treated samples was found to increase with respect to as-sprayed coatings, outperforming conventional high-velocity oxy-fuel (HVOF) deposits. Hardness was found to decrease after prolonged (<90 min) or higher temperature (>750 °C) exposures.

Keywords: amorphous metal; metallic glass; cold spray; XRD; EBSD

1. Introduction

Amorphous metals are drawing attention in several engineering fields owing to their unique physical, mechanical, and thermo-mechanical properties. In particular, Fe-based metallic glasses (MGs) are known to exhibit excellent soft-magnetic properties, wear and corrosion resistance, and can be produced at relatively low cost [1–8].

Bulk MGs are manufactured by different techniques, all including a rapid quenching step, yielding materials characterized by a short-range order but typically endowed with very limited ductility and with negligible plastic behavior in compression [9]. For these reasons, commercial applications of this class of materials are not yet consolidated.

Thermal-sprayed coatings of amorphous metals represent a viable alternative solution to producing MGs, while preserving their exceptional properties and avoiding extreme brittleness [9]. In fact, the lack of grain boundaries, representing the weak points of crystalline materials, can be responsible for improved resistance to wear and corrosion [10], and these protection properties can be easily conferred by surface layers deposited on tough and plastically deformable structural substrates. Metallic glasses can, therefore, represent the starting point for new functional materials with potential interesting applications in different fields of engineering.

Thermal-spray technologies are in principle suitable for depositing amorphous metal coatings, due to the very high cooling rates experienced by metal particles on impact with the substrate, and potentially able to avoid or limit crystallization.

In the last decades, different thermal-spray techniques, such as high-velocity oxy-fuel (HVOF), flame spray (FS), and plasma spray (PS), have been used to produce amorphous coatings [11–14]. However, several authors have reported partial crystallization and oxidation in amorphous coatings when HVOF, FS, and PS are used [11,15]. Crystallization and oxidation have both been reported to negatively affect the mechanical properties of the coatings [9].

Cold-gas spray (CGS) processes [16–18] have arisen and been consolidated in the last two decades as convenient alternatives to traditional thermal spraying, mainly due to the lower temperatures experienced by coating materials during the deposition process—limiting thermal impact on the substrate, reducing oxidation and chemical degradation on spraying, and allowing cold working of coatings during deposition—and to the very efficient mechanisms of adhesion, related either to the adiabatic shear instability [10,19] or to the hydrodynamic plasticity induced by pressure waves [20].

The aim of this paper is to explore the potential deposition of amorphous iron-based coatings by CGS, starting from commercially available powders with a chemical composition optimized for its glass-forming ability, investigating the effect of the very high kinetic energy content of solid particles on the crystallization tendency, even in the absence of extremely high cooling rates. Iron-based coatings of different compositions were already successfully deposited by List et al. [21], who also investigated the specific impact conditions to be met for the retainment of amorphous phases. For sake of comparison, the same powder was also used as feedstock material for the deposition of coatings by HVOF.

Partial or complete recrystallization of post-spraying thermal treatments were also attempted with the aim of investigating the effect of microstructure evolution on mechanical properties (mainly hardness) of CGS coatings.

2. Materials and Methods

A highly alloyed iron-based powder, produced by Nanosteel Company Inc., Providence, RI, USA, and identified by the commercial label SHS7574HVOF, was used as feedstock material, as already preliminarily reported in Reference [22]. The chemical composition of the alloy, containing boron, tungsten, and silicon, is optimized to favor the retainment of an amorphous structure on cooling. The actual chemical composition of the powder was determined by ICP-OES (inductively-coupled plasma optical emission spectrometry) analyses. Nominal and measured compositions are reported in Table 1.

Table 1. Chemical composition (nominal and measured by inductively-coupled plasma optical emission spectrometry (ICP-OES)) of the powder feedstock.

Weight %	Cr	C	B	Mo	W	Mn	Si	O	Fe
Nominal	<25	<2	<5	<15	<10	<2	<2	-	bal.
ICP-OES Analysis	18.55	0.97	3.3	12.88	6	1.6	1.57	0.018	

The powder's morphology and composition were characterized by D. Zois et al. [23,24], reporting a backscattered electron image of the particles [23] and microanalysis (energy dispersive spectroscopy elemental maps) of powder cross-sections [24]. It appears that the powder particles are mostly round-shaped, with a fraction of elongated particles, as typical of gas atomized feedstocks. The composition of the powder was found to be uniform, both among different particles and along particle diameter. Particles' size distribution was determined by laser diffraction equipment (MALVERN Mastersizer X, 30 s, ultrasonic bath, Malvern Panalytical, Malvern, UK), according to Fraunhofer diffraction theory. A deionized water/absolute ethanol mixture (50/50 by volume) medium was used for complete dispersion.

Starting from the measured chemical composition, the phases that were likely to be found in the material at thermodynamic equilibrium conditions were calculated using JMatPro[®] software (Sente Software Ltd., Surrey Research Park, UK) applying the database General Steel in the range from room temperature up to 1600 K.

Flat $50 \times 30 \times 3 \text{ mm}^3$ samples of AISI 304 stainless steel were coated using CGS equipment (IMPACT Spray System 5/11), with N_2 as the process gas. High-velocity oxy-fuel coatings were also deposited from the same feedstock material using TAFA JP 5000 equipment (Praxair Surface Technology, Indianapolis, IN, USA). Particles sprayed in these conditions attained partial/full melting before impact with the substrate. The CGS and HVOF process parameters are reported in Table 2. All the deposited coatings exhibited a thickness ranging between 500 and 600 μm .

Table 2. Cold-gas spraying (CGS) and high-velocity oxy-fuel (HVOF) deposition parameters.

CGS							
Process Gas	Gas Pressure (MPa)	Gas Flow Rate (m^3/h)	Gas Temperature ($^\circ\text{C}$)	Stand-off Distance (mm)	Torch Scanning Speed (mm/s)	Number of Spray Passes	Carrier Gas Flow Rate (m^3/h)
N_2	4	69	970	20	200	5	3
HVOF							
Barrel (mm)	O_2 Gas Flow Rate (m^3/h)	Kerosene Flow Rate (l/h)	Pressure in Combustion Chamber (MPa)	Stand-off Distance (mm)	Torch Scanning Speed (mm/s)	Number of Spray Passes	Carrier Gas Flow Rate (m^3/h)
101.6	48.14	272.55	0.696	355	500	15	0.66

Several samples deposited by CGS were heat-treated in a furnace under inert Ar atmosphere after spraying. Heat treatments were carried out varying the exposure temperature and time in the ranges 650–850 $^\circ\text{C}$ and 30–90 minutes, respectively.

Phase analysis of starting powders and of HVOF- and CGS-deposited coatings (both in as-sprayed and heat-treated conditions) was carried out by XRD (X-ray diffraction, Siemens D500, Bruker Corp., Billerica, MA, USA) in the 20–80 $^\circ$ 2θ range using $\text{Cu-}\alpha$ radiation (40 kV, 40 mA, 0.2 $^\circ$ steps, 1 s dwell time).

Microstructural analysis of as-sprayed and heat-treated coatings was carried out on cross-sections—after resin embedment, polishing, and etching—by SEM (scanning electron microscopy), using a SEM JSM 6480L apparatus (JEOL Ltd., Tokyo, Japan). Copper (II) chloride Kalling's etching was selected to give evidence of the ferritic phase, leaving carbides unaffected. Electron back scattered diffraction (EBSD) analysis was used (EBSD EDAX installed on a Zeiss EVO MA15 SEM) for final confirmation of the presence of an amorphous phase in the sprayed coatings. A focused ion beam (FIB) microscope (FEI Helios NanoLab 600 Dualbeam FIB/SEM, Thermo Scientific, Waltham, MA, USA) was used to extract thin slices of coatings for further observation and finer microstructural characterization by TEM (transmission electron microscopy; JEM 3200 FXHR, JEOL Ltd., Tokyo, Japan). Selected area diffraction (SAD) analysis was used to determine the crystallographic structure of the observed phases.

On the cross-sections of HVOF- and CGS-coated samples, both as-sprayed and heat-treated, dynamic indentation [25] measurements were carried out in order to evaluate contact hardness (HIT) according to the Oliver and Pharr method [26] (pre-load of 1.5 mN; loading rate of 20 mN/s; 30 s dwell at the maximum load; unloading rate of 20 mN/s). For each sample, 45 measurements were carried out for each load (0.5 and 1 N), using a Berkovich 3-sided penetrator.

3. Results and Discussion

3.1. Feedstock Powders and Coatings Characterization

Figure 1 shows the particle size distribution of the starting powder; an almost monomodal distribution can be assessed, centered around an average size of about 15 μm .

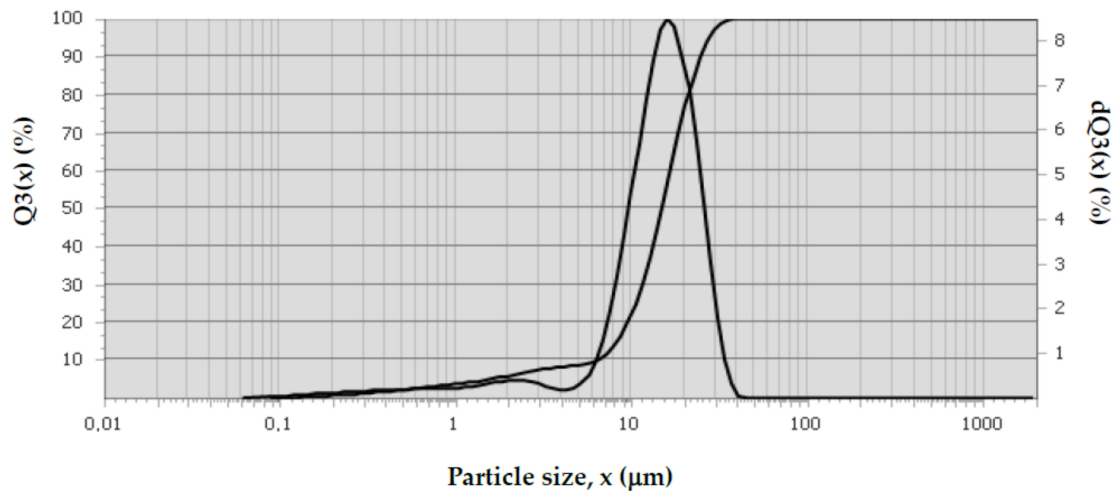


Figure 1. Particle size distribution of the starting powder (cumulative, left scale; integral, right scale).

Figure 2 reports the calculated phase composition of the coating material, at thermodynamic equilibrium conditions, as a function of temperature. The chemical composition of the investigated material contained a very high amount of B and C; at the thermodynamic equilibrium, three main phases were present: metallic Fe (ferrite or austenite, depending on the temperature), borides, and carbides. Iron-based alloys with similar composition typically showed an improved glass-forming ability (GFA) correlated to the nucleation of complex crystalline structures as a product of the first crystallization processes, thus increasing the thermal stability of super-cooled liquid [27]. For example, the formation of M_{23}C_6 precipitates occurred by a complex multistep crystallization process: amorphous \rightarrow long period structure \rightarrow χ -FeCrMo phase \rightarrow M_{23}C_6 , the latter having a unit cell of 116 atoms and involving the ordering of large portions of the amorphous structure.

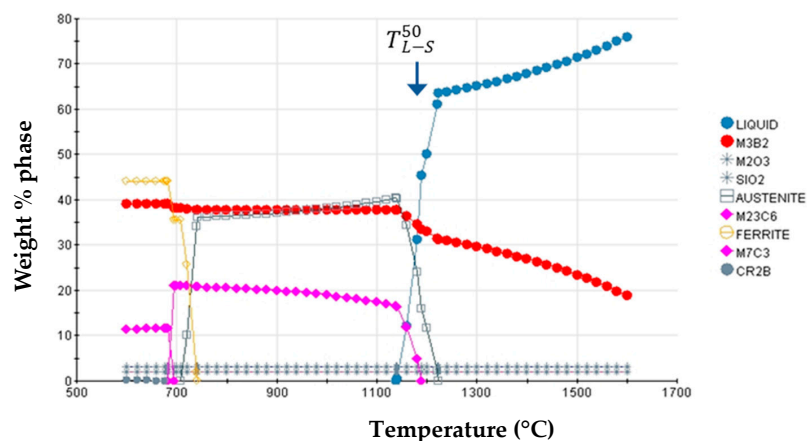


Figure 2. Calculated (JMatPro[®]) equilibrium phase composition of the coating material (Fe-19.48Cr-1.59Mn-16.68 Mo-2.33 O-1.49Si-6.64W-3.3B-0.97C, wt%) as a function of temperature.

The first consequence of this was that the crystallization kinetics were slow, as also demonstrated by the solidus temperature (1200 $^{\circ}\text{C}$), exceptionally low for a Fe-based alloy, suggesting that this composition was close to the deep eutectic of the Fe–C–B system, that greatly promotes the formation

of the amorphous metal because of the high thermodynamic stability and ordering of the liquid phase [28].

Therefore, if cooled rapidly (or if the energy of the system is efficiently dispersed by means of alternative mechanisms), this alloy is potentially suitable for assuming a nanocrystalline or even an amorphous microstructure.

This was confirmed by the XRD patterns reported in Figure 3, where the results of the phase analyses of the (a) starting powder, (b) HVOF, and (c) CGS-deposited coatings, in the as-sprayed conditions, are respectively reported.

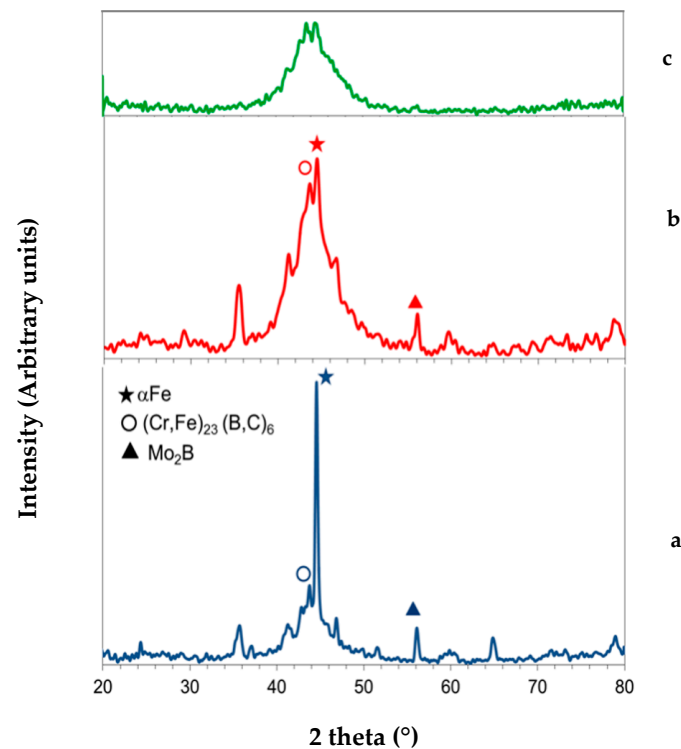


Figure 3. XRD patterns of (a) starting powder SHS7574; (b) HVOF-deposited coating; and (c) CGS-deposited coating.

The starting powders were characterized by the presence of thermodynamically stable crystalline $\alpha\text{-Fe}$, $(\text{Cr, Fe})_{23}\text{C}_6$ and M_2B phases; in the HVOF coating, the same phases were present, but the crystallization was not complete, or the attained grain size was much smaller (nanocrystalline), as indicated by the presence of broader and less defined peaks. In these two cases, the material processing temperature was higher than the liquidus (in the case of gas atomization of powders), or at least higher than the solidus (in the case of HVOF). Apparently, the cooling rate in these conditions was not sufficient to produce a complete amorphization, and the dominant phase was crystalline $\alpha\text{-Fe}$. The XRD pattern of the powder presented a higher crystalline fraction than the HVOF coating pattern, this was due to the difference in cooling rate experienced by the material in the two processes. In the case of the powders, heat was extracted from particles of about 15 μm in diameter by contact with a cold gas; in the case of the HVOF coating, more efficient cooling took place mainly by conduction from splats a few microns thick to the cold solid surface of the substrate.

In the case of CGS-deposited coatings, the XRD pattern shows the typical features of an amorphous material (very broad and low peaks centered around theoretical positions). The amorphous nature of the coating was also confirmed by the EBSD analysis reported in Figure 4. The Kikuchi lines, generated by the scattering on the lattice planes, can be clearly identified in the crystalline substrate, while they are absent in the coating, thus proving its amorphous state. A layered amorphous microstructure was observed in the SEM cross-section of the CGS coating, shown in Figure 4a. The layered morphology

was made of sprayed metallic particles partially flattened due to the combination of high-energy impact on the substrate and severe plastic deformation [29–31]. The powder particles' temperature during cold spraying did not attain solidus temperature, and the primary cause of amorphization in the CGS-deposited coating was, therefore, the high-strain/strain-rate deformation with shear instability [32] (due to the particles' high kinetic energy) rather than the rapid temperature decrease. It is well known that grain refinement up to nanocrystalline structures can be observed in materials submitted to a severe plastic deformation (SPD) process, such as e.g., accumulative roll bonding [33] or equal channel angular extrusion [34], where nanocrystalline structures are usually obtained. Also, in the case of CGS, the deformation on impact was so high as to completely destroy/avoid the crystalline structure, thus allowing the metastable formation of amorphous metals.

A thin slice of the CGS coating was extracted by FIB and observed by TEM in correspondence with the interlamellar contact between an amorphous splat and one of the very few nanocrystalline regions of the as-sprayed coating. Figure 5 reports the TEM image and the relative SAD patterns. As a further confirmation of the complex nature of the coating, in the SAD pattern of the region indicated as 1 in Figure 5a, a series of faint diffuse rings, typical of the amorphous phase, can be observed. On the other hand, in the region indicated with the number 2, the SAD pattern presents diffraction spots typical of a crystallized region.

Figure 6 shows a TEM image and SAD patterns corresponding to the crystallized region. As expected, TEM analysis confirms the presence of nano-crystalline α -Fe and micro-crystalline carbides and borides.

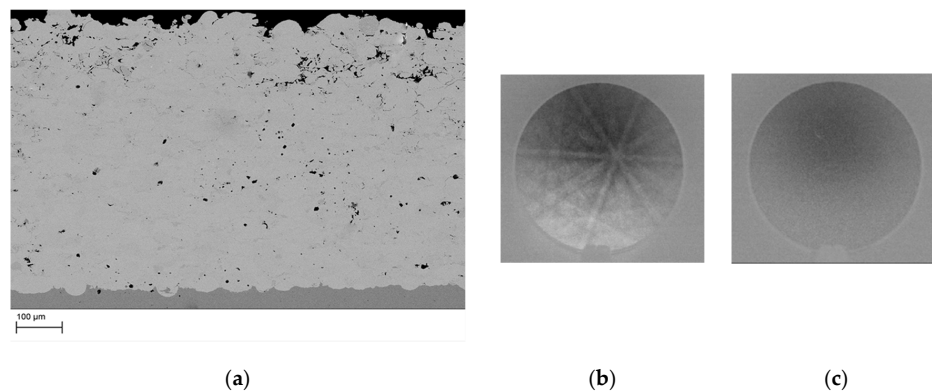


Figure 4. Results of EBSD analyses on a CGS coating in the as-sprayed condition: (a) cross-section of the sample as observed by SEM; (b) Kikuchi lines in the crystalline substrate, 1; (c) absence of Kikuchi lines in the amorphous coating, 2.

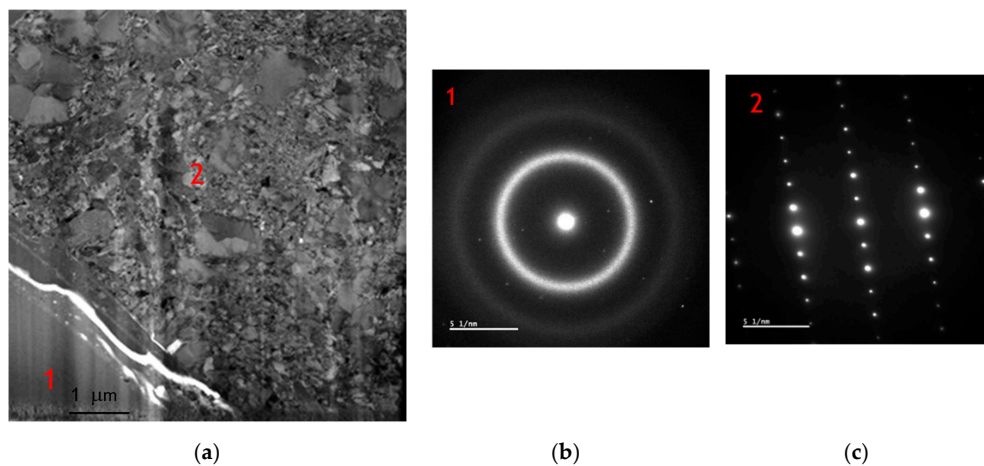


Figure 5. TEM image (a) and SAD patterns (b,c) of a CGS coating: 1. amorphous region; 2. crystallized region.

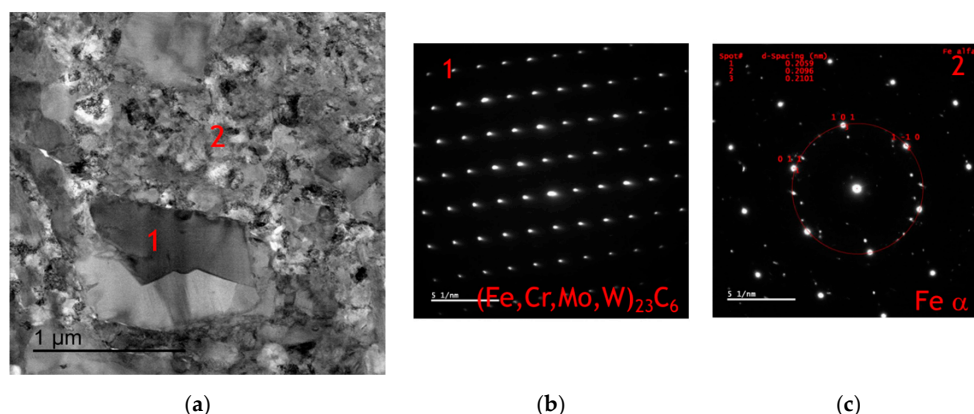


Figure 6. TEM image (a) and SAD patterns (b,c) in the crystallized region: 1. carbides; 2. Fe α .

3.2. Heat Treatment and Crystallization

Figure 7 shows the XRD patterns of CGS coatings before and after heat treatments carried out at 650, 750, and 850 °C for 90 minutes.

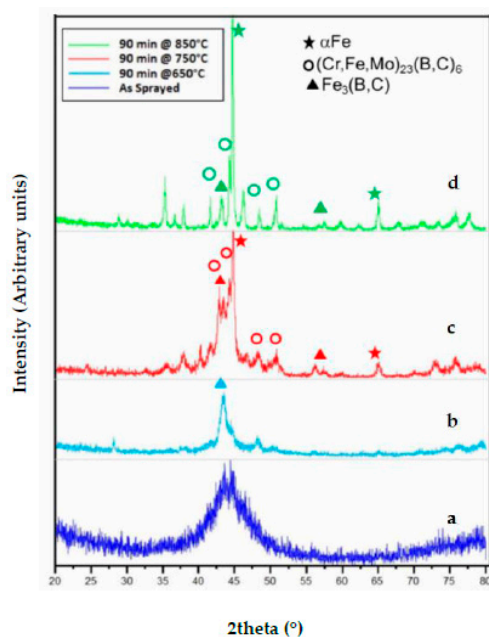


Figure 7. XRD patterns of CGS coatings: as-sprayed (a); heat-treated for 90 min at 650 °C (b); 750 °C (c); 850 °C (d).

Heat-treatment induced a partial crystallization, which was more evident as the treatment temperature increased. If the treatment temperature was lower than 700 °C (transition temperature between ferrite and austenite in the relevant alloy), the formation of carbides was the dominant phenomenon. At temperatures higher than 700 °C, the crystallization of the metallic phase was prevalent.

Figure 8 shows the cross-section of heat-treated CGS coatings observed by SEM, using backscattered electrons, after Kalling's etching (90 min heat treatment at 650 °C (a and d), 750 °C (b and e), and 850 °C (c and f)). Two kinds of splats were evidenced: the original rounded or flattened sprayed lamellae, characterized by the absence of any evident internal microstructuring, and the modified splats, appearing darker in the SEM images at low magnification, in which the presence of finer particles and precipitates of differentiated composition can be observed. The number of the splats belonging to the second type increased for increasing heat-treatment temperature. On the basis of

the gathered evidence, it seems that crystallization, as soon as it was triggered, spread rapidly to the whole splat, initially without affecting the surrounding splats (as evidenced in images at higher magnification). In the sample heat-treated at 850 °C, fine eutectic-like crystallization nuclei were observed, also in the initially unaffected splats (Figure 8c), suggesting that the attained temperature was sufficient to nucleate or extend crystallization to the entire coating.

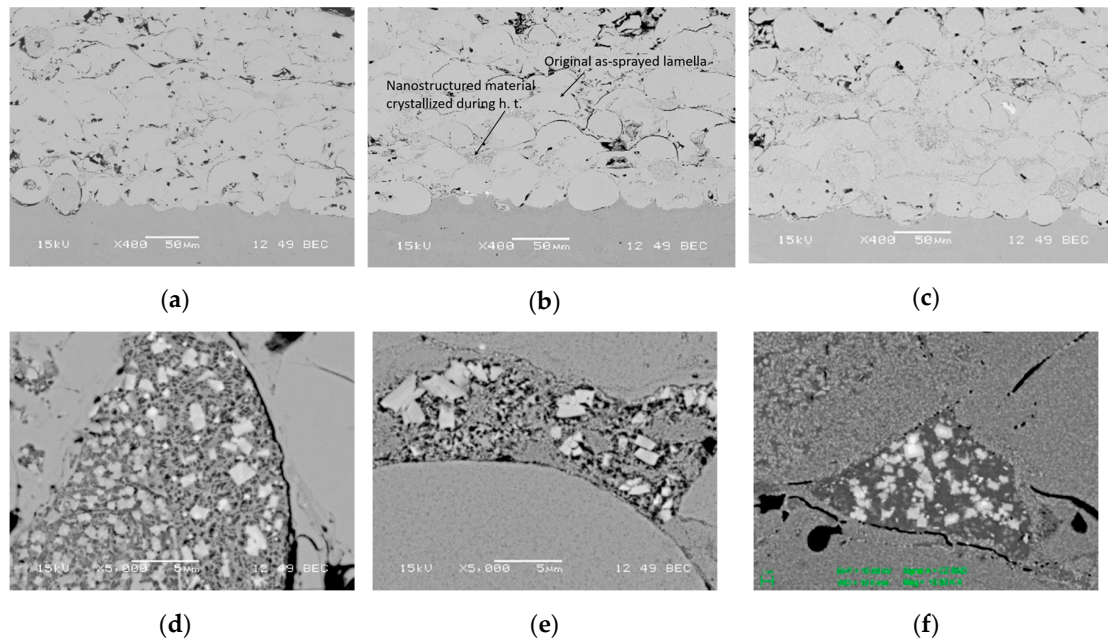


Figure 8. SEM micrographs of CGS coatings after Kalling's etching: (a,d) heat-treated at 650 °C; (b,e) heat-treated at 750 °C; and (c,f) heat-treated at 850 °C for 90 min. Original rounded or flattened light-colored lamellae and dark-colored regions, crystallized during heat treatment, can be recognized.

In Figure 9, contact hardness, measured with 0.5 and 1 N normal loads, of as-sprayed (HVOF and CGS) and heat-treated (CGS) coatings is reported. In the as-sprayed condition, HVOF coatings outperformed CGS deposits. This effect can be ascribed to the strengthening action of nanocrystalline domains and boundaries [28]. The same strengthening effect was observed on heat-treated CGS coatings, whose hardness increased for increasing temperatures in the range of 650–750 °C for shorter heat-treatment durations, and decreased again after prolonged treatment time or at higher exposure temperature, resulting in a sort of “over-aging” phenomenon. The observed phenomena can be explained on the basis of the well-known Hall-Petch [35] dependence-reversal effect [36], stating the existence of an optimal crystal size, usually of about a few tens of nm, corresponds to a peak hardness of the crystalline material.

When the first crystallization nuclei appear inside an amorphous material, hardness increases, and then decreases when, with the progression of crystallization, the grain size exceeds the optimal value.

Due to the complex multiphase structure of the investigated materials after heat treatment (composed by amorphous, fine Fe grains and coarser carbide and boride crystals), it was impossible to define a specific threshold value of the grain size for each coating and each heat treatment in order to quantitatively correlate the values' hardness to particular microstructural features.

However, more relevant and directly exploitable indications for specific industrial applications of interest can be drawn by the preliminary results just shown: hardness improvements of as high as approximately 54% can be obtained using cold-gas spraying instead of the more consolidated HVOF technique, provided a suitable partial crystallization heat treatment is carried out post-spraying, by carefully optimizing heat treatment temperatures (750 °C in the present case) and durations (90 min for the tested coating composition). On the other hand, should the amorphous nature of the coating

represent the most desirable feature for the examined application, as-sprayed cold-gas coatings could be the most appropriate and convenient material of choice.

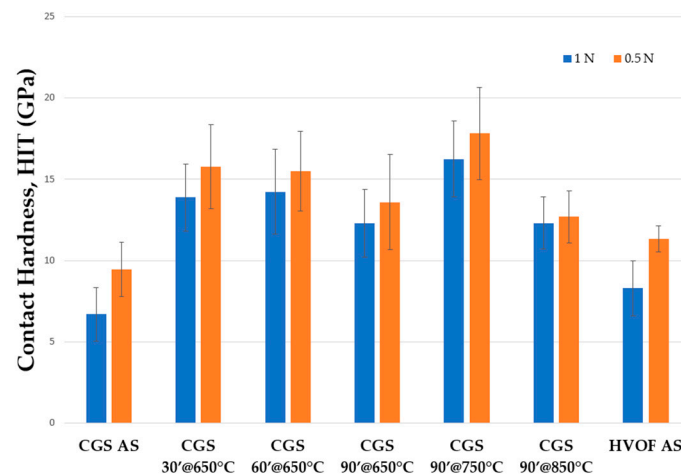


Figure 9. Contact hardness (HIT) of GGS and HVOF coatings, before (AS, as-sprayed) and after heat treatment, as measured by dynamic indentation.

4. Conclusions

It was shown that the deposition of amorphous Fe-based coatings using cold-gas spraying technology starting from appropriate composition feedstocks is a feasible process; material amorphization occurs as a consequence of severe mechanical strains induced by high particle kinetic energy rather than large temperature differences (rapid cooling), as is the case with other spray deposition techniques (e.g., HVOF).

Amorphous coatings can either be used in the as-sprayed condition (provided they are not exposed to high temperature in operation) or they can be suitably heat-treated at temperatures higher than 650 °C, so that nanometric size crystals are nucleated in the desired amount between amorphous lamellae, thus improving hardness, and presumably, mechanical/wear resistance properties of the coatings.

According to the gathered and discussed experimental evidence, as soon as crystallization was triggered in the high-energy regions of the coating (mainly in interlamellar contacts), it was rapidly spread to the whole splat, without initially affecting the surrounding splats. This gives place to a “bimodal”-like structure, that has often been proved very effective in providing appropriate compromises between hardness and toughness [37,38].

The comparison of the electrochemical and high-temperature corrosion behavior of as-sprayed and partially recrystallized cold-gas coatings and conventional HVOF deposits will be the subject of future investigation.

Author Contributions: Conceptualization, M.T., F.M., G.P.; Data curation, C.B., F.M., S.M., G.P.; Investigation, M.T., A.B., A.L.M., F.M., S.M., G.P.; Methodology, M.T.; Project administration, M.T., F.M., G.P.; Supervision, C.B., M.T.; Writing—Original Draft, M.T., C.B.; Writing—Revision, C.B., G.P.

Funding: The research activities were carried out in the frame of the EOMAT project (PON03PE_00092_1) funded by the Italian Minister for University and Research.

Conflicts of Interest: The authors declare no conflict of interest.

References

1. Yoon, S.; Kim, J.; Bae, G.; Kim, B.; Lee, C. Formation of coating and tribological behavior of kinetic sprayed Fe-based bulk metallic glass. *J. Alloys Compd.* **2011**, *509*, 347–353. [[CrossRef](#)]

2. Keryvin, V.; Hoang, V.H.; Shen, J. Hardness, toughness, brittleness and cracking systems in an iron-based bulk metallic glass by indentation. *Intermetallics* **2009**, *17*, 211–217. [[CrossRef](#)]
3. Inoue, A.; Shen, B.L.; Chang, C.T. Super-high strength of over 4000 MPa for Fe-based bulk glassy alloys in [(Fe_{1-x}Co_x)_{0.75}B_{0.2}Si_{0.05}]₉₆Nb₄ system. *Acta Mater.* **2004**, *52*, 4093–4099. [[CrossRef](#)]
4. Pang, S.J.; Zhang, T.; Asami, K.; Inoue, A. Bulk glassy Fe-Cr-Mo-C-B alloys with high corrosion resistance. *Corros. Sci.* **2002**, *44*, 1847–1856. [[CrossRef](#)]
5. Makino, A.; Bitoh, T.; Kojima, A.; Inoue, A.; Masumoto, T. Magnetic properties of zero-magnetostrictive nanocrystalline Fe-Zr-Nb-B soft magnetic alloys with high magnetic induction. *J. Magn. Magn. Mater.* **2000**, *215–216*, 288–292. [[CrossRef](#)]
6. Trexler, M.M.; Thadhani, N.N. Mechanical properties of bulk metallic glasses. *Prog. Mater. Sci.* **2010**, *55*, 759–893. [[CrossRef](#)]
7. Kaban, I.; Jovari, P.; Waske, A.; Stoica, M.; Bednarcik, J.; Beuneu, B.; Mattern, N.; Ecker, J. Atomic structure and magnetic properties of Fe-Nb-B metallic glasses. *J. Alloys Compd.* **2014**, *586*, S189–S193. [[CrossRef](#)]
8. Wang, W.H.; Dong, C.; Shek, C.H. Bulk metallic glasses. *Mater. Sci. Eng. R* **2004**, *44*, 45–89. [[CrossRef](#)]
9. Henao, J.; Concustell, A.; Cano, I.G.; Cinca, N.; Dosta, S.; Guilemany, J.M. Influence of Cold Gas Spray process conditions on the microstructure of Fe-based amorphous coatings. *J. Alloys Compd.* **2015**, *622*, 995–999. [[CrossRef](#)]
10. Bae, G.; Xiong, Y.; Kumar, S.; Kang, K.; Lee, C. General aspects of interface bonding in kinetic sprayed coatings. *Acta Mater.* **2008**, *56*, 4858–4868. [[CrossRef](#)]
11. Miura, H.; Isa, S.; Omuro, K. Production of Amorphous Iron-Nickel Based Alloys by Flame-Spray Quenching and Coatings on Metal Substrates. *Trans. Jpn. Inst. Met* **1984**, *25*, 284–291. [[CrossRef](#)]
12. Voyer, J. Surface Wear Improvement of Al-Alloys by Amorphous Iron-Based Flame-Sprayed Coatings. *Mater. Sci. Forum* **2011**, *690*, 405–408. [[CrossRef](#)]
13. Liu, X.Q.; Zheng, Y.G.; Chang, X.C.; Hou, W.L.; Wang, J.Q. Influence of HVOF Thermal Spray Process on the Microstructures and Properties of Fe-based Amorphous/Nano metallic Coatings. *Mater. Sci. Forum* **2010**, *633–634*, 685–694. [[CrossRef](#)]
14. Zhang, C.; Liu, L.; Chan, K.C.; Chen, Q.; Tang, C.Y. Wear behavior of HVOF-sprayed Fe-based amorphous coatings. *Intermetallics* **2012**, *29*, 80–85. [[CrossRef](#)]
15. Choi, J.H.; Lee, C.; Lee, D.B. Oxidation behavior of bulk amorphous Ni₅₇Ti₁₈Zr₂₀Si₃Sn₂ coatings between 473 and 973 K in air. *J. Alloys Compd.* **2008**, *449*, 384–388. [[CrossRef](#)]
16. Raelison, R.N.; Xie, Y.; Sapanathan, T.; Planche, M.P.; Kromer, R.; Costil, S.; Langlade, C. Cold gas dynamic spray technology: A comprehensive review of processing conditions for various technological developments till to date. *Addit. Manuf.* **2018**, *19*, 134–159. [[CrossRef](#)]
17. Champagne, V.; Helfrich, D. The unique abilities of cold spray deposition. *Intern. Mater. Rev.* **2016**, *61*, 437–455. [[CrossRef](#)]
18. Grujicic, M.; Zhao, C.L.; De Rosset, W.S.; Helfrich, D. Adiabatic shear instability based mechanism for particles/substrate bonding in the cold-gas dynamic-spray process. *Mater. Des.* **2004**, *25*, 681–688.
19. Drehmann, R.; Grund, T.; Lampke, T.; Wielage, B.; Manygoats, K.; Schucknecht, T.; Rafaja, D. Splat formation and adhesion mechanisms of cold gas-sprayed Al coatings on Al₂O₃ substrates. *J. Therm. Spray Technol.* **2014**, *23*, 68–75. [[CrossRef](#)]
20. Hassani-Gangaraj, M.; Veysset, D.; Champagne, V.K.; Nelson, K.A.; Schuh, C.A. Adiabatic shear instability is not necessary for adhesion in cold spray. *Acta Mater.* **2018**, *158*, 430–439. [[CrossRef](#)]
21. List, A.; Gärtner, F.; Schmidt, T.; Klassen, T. Impact conditions for cold spraying of hard metallic glasses. *J. Therm. Spray Technol.* **2012**, *21*, 531–540. [[CrossRef](#)]
22. Tului, M.; Bezzon, A.; Marino, A.; Marra, F.; Matera, S.; Pulci, G. Amorphous steel coatings deposited by HVOF and Cold Gas Spray processes. In Proceedings of the International Thermal Spray Conference, DVS Media GmbH, Dusseldorf, Germany, 7–9 June 2017; pp. 737–740.
23. Zois, D.; Lekatou, A.; Vardavoulias, M.; Vaimakis, T.; Karantzalis, A.E. Partially amorphous stainless steel coatings: Microstructure, annealing behavior and statistical optimization of spray parameters. *Surf. Coat. Tech.* **2011**, *206*, 1469–1483. [[CrossRef](#)]
24. Zois, D.; Lekatou, A.; Vardavoulias, M. Preparation and characterization of highly amorphous HVOF stainless steel coatings. *J. Alloys Compd.* **2010**, *504S*, S283–S287. [[CrossRef](#)]

25. ISO 14577. *Instrumented Indentation Test for Hardness and Materials Parameters*; International Organization for Standardization: Genève, Switzerland, 2007.
26. Oliver, W.C.; Pharr, G.M. An improved technique for determining hardness and elastic modulus using load and displacement sensing indentation experiments. *J. Mater. Res.* **1992**, *7*, 1564–1583. [[CrossRef](#)]
27. Lu, Z.P.; Liu, C.T.; Thompson, J.R.; Porter, W.D. Structural amorphous steels. *Phys. Rev. Lett.* **2004**, *92*, 245503. [[CrossRef](#)] [[PubMed](#)]
28. Hirata, A.; Hirotsu, Y.; Amiya, K.; Inoue, A. Crystallization process and glass stability of an Fe₄₈Cr₁₅Mo₁₄C₁₅B₆Tm₂ bulk metallic glass. *Phys Rev. B Condens Matter Mater Phys.* **2008**, *78*, 144205. [[CrossRef](#)]
29. Davis, J.R. *Handbook of Thermal Spray Technology*; ASM International: Materials Park, OH, USA, 2004; pp. 47–53, 77–84.
30. Cavaliere, P. Cold Spray Coating Technology for Metallic Components Repairing. In *Through life Engineering Services*; Redding, L., Roy, R., Eds.; Springer International Publishing: Cham, Switzerland, 2015; pp. 175–184.
31. Hussain, T.; McCartney, D.G.; Shipway, P.H.; Zhang, D. Bonding Mechanisms in Cold Spraying: The Contributions of Metallurgical and Mechanical Components. *J. Therm. Spray Technol.* **2009**, *18*, 364–379. [[CrossRef](#)]
32. Lee, C.; Kim, J. Microstructure of Kinetic Spray Coatings: A Review. *J. Therm. Spray Technol.* **2015**, *24*, 592–610. [[CrossRef](#)]
33. Tsuji, N.; Saito, Y.; Lee, S.-H.; Minamino, Y. ARB (Accumulative Roll-Bonding) and other new Techniques to Produce Bulk Ultrafine Grained Materials. *Adv. Eng. Mater.* **2003**, *5*, 338–344. [[CrossRef](#)]
34. Song, M.; Sun, C.; Chen, Y.; Shang, Z.; Li, J.; Fan, Z.; Hartwig, K.T.; Zhang, X. Grain refinement mechanisms and strength-hardness correlation of ultra-fine grained grade steel processed by equal channel angular extrusion. *Int. J. Pres. Ves. Pip.* **2019**, *172*, 212–219. [[CrossRef](#)]
35. Hansen, N. Hall-Petch relation and boundary strengthening. *Scr. Mater.* **2004**, *51*, 801–806. [[CrossRef](#)]
36. Whang, S.H. (Ed.) *Nanostructured Metals and Alloys: Processing, Microstructure, Mechanical Properties and Applications*; Woodhead Publishing: Cambridge, UK, 2011; p. 299.
37. Baiamonte, L.; Marra, F.; Pulci, G.; Tirillò, J.; Sarasini, F.; Bartuli, C.; Valente, T. High temperature mechanical characterization of plasma-sprayed zirconia-yttria from conventional and nanostructured powders. *Surf. Coat. Tech.* **2015**, *277*, 289–298. [[CrossRef](#)]
38. Lima, R.S.; Kucuk, A.; Berndt, C.C. Bimodal distribution of mechanical properties on plasma sprayed nanostructured partially stabilized zirconia. *Mater. Sci. Eng. A* **2002**, *27*, 224–232. [[CrossRef](#)]



© 2019 by the authors. Licensee MDPI, Basel, Switzerland. This article is an open access article distributed under the terms and conditions of the Creative Commons Attribution (CC BY) license (<http://creativecommons.org/licenses/by/4.0/>).